

Diversity of Nanofibers from Electrospinning: from Graphitic Carbons to Ternary Oxides.

Yu Wang, Idalia Ramos and Jorge J. Santiago-Aviles
*University of Pennsylvania and University of Puerto Rico at Humacao,
Philadelphia, PA, USA and Humacao, PR,
USA*

1. Introduction

Electrospinning is a simple method of obtaining polymer fibers with nanoscopic diameter. It uses electrical forces to produce polymer fibers with nanometer scale diameters. Electrospinning occurs when the electrical forces at the surface of an organic solution or melt overcome the surface tension and cause an electrically charged jet to be ejected. As the the solvent evaporates, an electrically charged fiber remains. This charged fiber can be directed by electrical forces and then collected in sheets or other useful geometrically forms. In this monograph we are exploring the use of electrospinning in the generation of nanoscopic and microscopic fibers of conductors such as graphitic carbons, semiconductors such as SnO_2 , and insulators such as the Perovskite PZT. The discussion will center mostly in the fibers electrical properties and it applications.

Carbon Nanofibers: Carbon nanofibers, like other quasi-one-dimensional nanostructures such as nanowires, nanotubes and molecular wires have potential application in a multiplicity of fields, such as high-temperature catalysis, heat-management materials in aircraft, and filters for separation of small particles from gas or liquid. Of more importance to us, there is a possible use as building blocks for bottom-up assembly applications in nanoelectronics and photonics [Mrozowski, 1979; Hu et al, 1999; Duan et al, 2001] Carbon fibers are usually produced by spinning from organic precursor fibers or by chemical vapor deposition (CVD). While the spinning method can only produce microscale carbon fibers, CVD can synthesize carbon fibers with diameters from several microns down to less than 100 nm [Bahl et al, 1998; Endo et al, 2001]. However, CVD involves a complicated process and high cost. Electrostatic generation, or electrospinning technique, invented in the 1930s [Formhals,1934], recently gained renewed interest because it can spin a variety of ultrafine polymer fibers in a micro- or even nanoscale at low cost [Doshi & Reneker, 1995]. By simply pyrolyzing electrospun ultrafine polymer fibers, with a subsequent heat treatment, Chun et al. [Reneker & Chun, 1996] and the authors [Wang et al, 2003] have obtained carbon nanofibers. In general, carbons may include classic carbons such as soot, charcoal, graphite, and “new” carbons. Among the new variants we can mention carbon fibers derived from polyacrylonitrile (PAN), and glass-like carbons derived from nongraphitizable precursors, i.e., various types of more or less crystallized polycrystalline graphites [Iganaki & Radovic, 2002]. These building techniques could overcome fundamental limitations of conventional microfabrication based on lithography [Hu et al, 1999; Duan et al, 2001].

Source: Nanofibers, Book edited by: Ashok Kumar,
ISBN 978-953-7619-86-2, pp. 438, February 2010, INTECH, Croatia, download from SCIYO.COM

Carbon fibers have wide applications in structural materials such as composites, and potentially in a multiplicity of nonstructural applications such as sensors [Rebouillat et al, 1999]. The recent "rediscovery" of electrostatic deposition has enabled one to spin a variety of ultra-fine polymer fibers in a simple way, which can be heat treated into carbon fibers with diameter in the nanoscale range [Doshi & Reneker, 1995; Reneker & Chung, 1996; Wang et al, 2002]. The application of carbon nanofibers as sensing elements relies on their electronic transport properties being modulated by the sensing element physico-chemical interaction with the analyte. The authors recently evaluated the size of single electrospun polyacrylonitrile (PAN)-derived carbon nanofibers using a scanning probe microscope for measuring their conductivity at room temperature, and found that the conductivity depends on annealing temperature and time [Wang et al, 2003]

It is well known that the electrical conductivity of pyrolytic graphite increases with temperature. Such temperature dependence was at first explained by the simple two-band (STB) model [Klein, 1964]. The STB model also predicts a level off of the conductivity at a very low temperature. However, recent experimental results show that the conductivity of carbon fibers is very sensitive to temperature at very low values (K) [Bright & Singer, 1979; Spain et al, 1983; Koike & Fukase, 1987]. Such anomaly has been attributed to weak electron localization [Koike & Fukase, 1987], electron-electron interaction [Koike & Fukase, 1987], the Kondo effect [Koike & Fukase, 1987], and hopping mechanism [Baker & Bragg, 1983], all of which show very weak effects unless evaluated at very low temperatures. As to the overall temperature dependence of conductivity, two-dimensional (2-D) weak localization, hopping and tunneling [Abeles et al, 1975] mechanisms have been put forward as possible explanations.

Although classical electron transport theory predicts an increase of electrical resistance in the presence of a magnetic field [Putley, 1960], Mrozowski and Chaberski found a decrease of resistance with magnetic field, or negative magnetoresistance, in partially ordered (pregraphitic) carbons [Mrozowski & Chaberski, 1956]. Since then, negative magnetoresistance has been found not only in poorly graphitized bulk carbon [Hishiyama, 1996] and carbon thin film [Faist & Lohneysen, 2002], but also in carbon fibers, irrespective of whether the carbon fibers were derived from PAN [Koike & Fukase, 1987], benzene [Endo et al, 1982], pitch-derived [Bright & Singer, 1979], or CVD [Fuji et al, 2002]. The most commonly accepted model accounting for the negative magnetoresistance was Bright's model [Bright, 1979]. This model attributes the resistance decrease to the increase of the density of the states and carrier density with magnetic field, arising from the formation of Landau levels. However, the Bright model cannot account for all of the observed phenomena, including the strong temperature dependence of magnetoresistance below liquid-helium temperature, and the absence of magneto-resistance saturation at high-magnetic field. Then, Bayot et al. [Bayot et al, 1984, 1990] explained the effect using a weak-localization mechanism, which results as a consequence of any small disorder in the electronic system. The weak-localization effects in pregraphitic carbon fibers are due to their turbostratic phase structure, in prior 2-D.

It is noteworthy that the anomalous temperature and magnetic field dependence of conductivity have been found in carbon fibers with diameters larger than 10 nm. It is interesting to evaluate the scaling of such effects, that is, whether similar effects exist in carbon fibers with a diameter of nanoscale although such evaluation becomes increasingly difficult as the diameter is reduced. Note that most of the investigated carbon fibers were heat treatment temperature was higher than 1000 °C, with their observed negative

magnetoresistance of a few percents in magnitude. The weak localization in carbon fiber originates from its disordered nature. By lowering the carbonization temperature, we can probe a lower degree of order in the carbon fiber, and may observe a stronger weak localization effect. In this chapter we comment on the temperature dependence of the electrical conductivity of carbon nanofiber pyrolyzed at a lower temperature of 1273 K, its large negative magnetoresistance at low temperature, and attempt to explain such properties within the frame work of STB and 2D weak-localization models.

Oxide fibers

Binary oxides fibers: Semiconducting tin oxide (stannic oxide, SnO_2), with a rutile structure and a wide bandgap ($E_g = 3.6$ eV), is chemically inert, mechanically hard, thermally heat-resistant and has a wide variety of existing and potential applications in sensors and optoelectronics such as solar cells, displays and electrochromic devices [Chopra et al, 1983; Williams, 1987]. While the optoelectronics applications of the oxide are mostly due to its wide bandgap, which makes it transparent up to ultraviolet light, its sensor applications are derived from its conductivity modulation by species chemisorbed on its surface and their interaction with non-stoichiometric oxygen vacancies in its lattice. Although the two kinds of applications require SnO_2 with different nature and levels of crystal defects, such as dopants and oxygen vacancies, both have taken advantage of the thin film morphology, and therefore SnO_2 thin film has been a research focus. So far, the thin film has been synthesized by various methods, such as evaporation [Seal & Shukla, 2002], sputtering [Shuah & Fun, 1986], spray pyrolysis [Sinclair et al, 1965], chemical vapor deposition [Santhi et al, 1980] and the sol-gel process [Davazoglou, 1997], and its synthetic processes have been characterized and correlated to its final stoichiometry, phase constituents and crystal defects. The preference for thin films in sensor applications is due to its higher surface-to volume ratio than that of the bulk shape and its restriction to the grain growth perpendicular to the substrate. The ratio is even higher and the grain growth is further confined for a fibrous shape. Unfortunately, SnO_2 fiber has been synthesized in only a limited number of ways, such as by laser ablation [Mishra et al, 2002], thermal decomposition [Liu et al, 2003], oxidizing electrodeposition of a template [Xu et al, 2002] and electrospinning [Kolmakov, 2003]. Of these methods, electrospinning is especially interesting in that it is easy, inexpensive, versatile and flexible. The technique was invented as early as the 1930s [Li et al, 2003] and was recently revitalized to synthesize ultra-fine polymer fibers. We were the first to report the synthesis of micro- and nanoscopic inorganic (lead zirconate titanate) fibers using electrospinning [Wang et al, 2004, Wang & Santiago-Aviles, 2002] and we also developed two recipes for the electrospinning of SnO_2 fibers: one was modified from that of SnO_2 thin film fabrication through the sol-gel route [Wang & Santiago-Aviles, 2004] and the other, developed independently, thermally decomposes a single metal-organic, dimethyldineodecanoate tin

($\text{C}_{22}\text{H}_{44}\text{O}_4\text{Sn}$), mixed with a solution of poly (ethylene oxide) (PEO, $\text{HO}-(\text{CH}_2-\text{CH}_2-\text{O})_n-\text{H}$) in chloroform (CHCl_3). The $\text{C}_{22}\text{H}_{44}\text{O}_4\text{Sn}$ compound was chosen because it is inexpensive, commercially available, neither too toxic nor too harmful to the environment and, most importantly, has appropriate rheological properties, especially when it is mixed with PEO/ CHCl_3 solution for electrospinning [Wang et al, 2005]. The second recipe can further introduce pores to fibres as to enhance their ratio of surface area to volume. Such porous SnO_2 fibres have electrical properties highly sensitive to their environment [Wang et al, 2004]. Since the precursor solution ($\text{C}_{22}\text{H}_{44}\text{O}_4\text{Sn} / \text{PEO} / \text{CHCl}_3$) contains organic groups and Sn-C and Sn-O bonds that are infrared-active, Fourier-transform infrared (FTIR)

spectroscopy will be an effective way to reveal changes in their structure and atomic bonding. This paper uses FTIR, together with thermogravimetric (TG) and differential thermal (DT) analysis (TGA and DTA) and x-ray diffraction (XRD) to further identify the synthesized fibres and to reveal a series of changes that lead to the conversion of the starting chemicals into the final product of porous ultra-fine SnO₂ fibres. This information will help us to control and tailor the micro/nanostructure, porosity and lattice defects of the final SnO₂ fibres so as to meet different specific application requirements.

Transparent conductive oxides (TCOs) have received extensive attention because of their important optoelectronic applications such as electrochromic devices, heat mirrors, and transparent electrodes and antireflection coatings in solar cells. Usually such oxides are semiconductors and their transparency is due to their wide band gap [Wang et al, 2007]. Tin oxide or stannic oxide (SnO₂) is a typical TCO. With a wide band gap of around 3.6eV makes it transparent up to the ultra-violet (UV) light. Although intrinsic stoichiometric single crystal SnO₂ is an insulator, its conductivity can be greatly increased either by impurity doping or by the introduction of oxygen vacancies in its lattice, which donate electrons [Chopra et al, 1983]. Since most optoelectronic, as well as sensing, applications prefer a thin film shape [Chopra et al, 1983; Jarzebski & Marton, 1976], SnO₂ thin films have been synthesized by numerous methods, such as chemical vapor deposition [Davazoglou, 1997], sol-gel [Terrier et al, 1997], spray pyrolysis [Shanti et al, 1999] and polymeric precursor [Giraldi et al, 2006], and their electrical and optical properties have been well characterized [Davazoglou, 1997; Giraldi et al, 2006]. However, for many applications such as a line light source, a fibrous shape is required. Unfortunately, so far only a few methods, namely, thermal decomposition [Xu et al, 2002], laser ablation [Liu et al, 2003], template oxidation [Kolmakov et al, 2003], vapor deposition [Mathur et al, 2005] and electrospinning [Wang et al, 2004,2005], have been developed to fabricate SnO₂ nanofibers or ribbons and their optical properties have been only barely touched [Liu et al, 2004; Dharmaraj et al, 2006] even though such properties characterization is indispensable for their applications. To our knowledge, no report has been made on characterizing their optical band gap, the most important parameter for their optoelectronic applications. The authors of this article have developed two recipes for electrospinning SnO₂ fibers [Wang et al, 2004,2005] and characterized their electrical properties. We investigate their optical and photoconductive properties, with the emphasis on the determination of their optical band gap and conductance response to UV light.

Binary oxide semiconductors have important sensing and optoelectronic applications [Seal & Chukla, 2002; Batzil & Diebold, 2005]. Usually, such oxides have a wide band gap and are good insulators in their undoped and stoichiometric state. However, oxygen vacancies leading to nonstoichiometry can easily be formed in their lattice, donate electrons, and greatly increase their conductivity. Their conductivity is also modulated by species chemisorbed on their surface and the subsequent interaction between the chemisorbed species and the nonstoichiometric oxygen vacancies. We fabricated nanofibers using electrospinning and metallorganics decomposition (MOD) techniques [Wang et al, 2004, 2007]. The conductivity of our synthesized fiber is highly sensitive to its environment, suggesting promising sensing applications. In this letter, we fabricated a gas sensor based on a single electrospun SnO₂ nanofiber and used it to detect moisture, and methanol gases. Although nanowires fabricated in other ways have been used to detect CO, and other gases [Kolmakov et al, 2003], this might be one of the earliest such use using electrospun fibers.

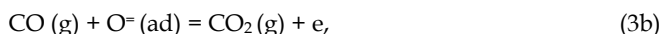
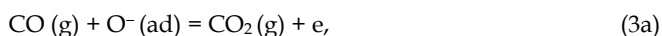
Civilian and industrial safety control, environmental protection and homeland security have stimulated great demand for novel chemical sensors, including gas sensors that can monitor a small amount of toxic, inflammable and/or explosive gases such as hydrogen (H₂) and carbon monoxide (CO) and odorous components such as O₃ and NO_x. The core element in a gas sensor is its sensing material. Binary oxide semiconductors constitute a promising family of sensing materials used in gas sensors because they are cost-effective, chemically inert, mechanically hard, and thermally heat-resistant, and therefore can be used in a harsh environment and are reliable over a long term [Williams, 1987; Seal & Chukla, 2002; Batzill & Diebold, 2005]. Electrically, they have a wide band gap and are good insulators if they are pure and stoichiometric. However, point defects, such as oxygen vacancies, can easily form in their lattice leading to non-stoichiometry, and act as donors as depicted below.



Such interactions greatly increase their conductivity. On the other hand, environmental oxygen atoms can be adsorbed on their surface, pick up electrons from the conduction band,



This chemisorption leads to a positively charged layer due to electron depletion immediately below the negatively charged surface and greatly decreasing their conductivity. When the surface is exposed to a reductive gas such as CO, however, the surface-adsorbed O^{·-} or O⁼ ions will react with the reducing gas molecules, release electrons,



Leading to a decrease of the depletion zone, and greatly increasing the conductivity. Such conductivity modulation by surface chemisorbed species and their interaction with the point defects provides a reliable gas detecting mechanism for binary oxide gas sensors [Williams, 1987; Seal & Chukla, 2002; Batzill & Diebold, 2005]

Tin oxide (SnO₂) sensors represent some of the early-commercialized chemical sensors (the Taguchi sensor [Naoyoshi, 1975]). Usually the SnO₂ sensing element is used in the shape of a thin film [Capone et al, 2001; Mandayo et al, 2003; Korotchenkov et al, 1999] because of its inherent higher surface-to-volume ratio than bulk. A fibrous or ribbon shape is more favorable for surface sensing than bulk and thin films in that it has an even higher surface-to-volume ratio. The ratio can also be increased by the introduction of pores into the SnO₂ thin film [Jin et al, 1998]. So, porous nanofiber/nanoribbon will be doubly favorable for surface sensing. Unfortunately, these had not been synthesized until recently, when we fabricated porous SnO₂ ribbons, with horizontal and vertical dimensions of 100 nm–20 μm and 10–100 nm, respectively, from the metallo-organic precursor dimethyldiiododecanoate tin (C₂₂H₄₄O₄Sn) using electrospinning and thermal decomposition techniques [Wang et al, 2004, 2007]. As SnO₂ gas sensors are usually used in atmosphere above room temperature for maximum sensitivity, it is essential to evaluate the electrical conductance (G) of our SnO₂ nanoribbons in analyte gas atmosphere. We also want to find its temperature (T)

dependence between room temperature and its probable elevated operating temperature, which is usually 473 to 773 K [Williams, 1987; Seal & Chukla, 2002; Batzill & Diebold, 2005]. Previous studies on bulk and thin-film SnO₂ has demonstrated that, due to the temperature-sensitive thermodynamics of surface chemisorption/desorption and surface-lattice interaction, conductance is dictated by the temperature to a large extent [Jarzebski & Marton, 1976; Ryzhikov et al, 2003]. In this chapter we briefly explored the electrical conductance of our single electrospun porous nanoribbon and its T-dependence in ambient air, and hopefully paves the way for potential sensing applications.

Ternary and more complex oxide fibers: Lead zirconate titanate, Pb (Zr_xTi_{1-x}) O₃ (PZT), is a well-known ferroelectric material with significant technological importance [Yoshikawa et al, 1995]. PZT fibers have potential for utilization in high performance hydrophones and ultrasonic transducer applications [Yoshikawa et al, 1995]. The author's group synthesized PZT fibers with diameter from 100 nm to 20 μm by means of electrospinning and metallo-organic decomposition [Wang et al, 2002; Wang & Santiago-Aviles, 2004]. Since then, it has been a challenge for us to evaluate their ferro electric properties. Usually, PZT is evaluated as dielectric media in a sandwiched metal/PZT/ metal capacitor [Trolier-Mckinstry & Murali, 2004]. Such evaluation does not work for a single PZT fiber with diameter less than 10 μm because of its ultra low capacitance. Recently, piezoresponse imaging (PRI) has been developed to probe polarization domains in ferro-electric thin films (including PZT thin film), measure their properties in micro- or nano-scale, and correlate domain polarization and local properties directly with topography and morphology [Birk et al, 1991; Harnagea, 2007]. We will explore the use of such techniques in elucidating PZT properties.

2. Experimental details

Carbon Nanofibers: The fibers precursor is a commercial polyacrylonitrile (PAN) and N, N-dimethyl formamide (DMF) solution, in a ratio of 600 mg PAN to 10 ml DMF. The solution was deposited on silicon wafers with a 150-nm-thick film of silicon oxide and patterned with 1 X 1 mm² gold contact array. A homemade electrospinning setup [Wang et al, 2003], was used to spin single precursor fibers between two isolated gold contacts (Fig. b). The as-spun PAN fibers were pyrolyzed and heat treated at 1273 K for 30 min in a vacuum of 10⁻⁶ torr. The processed fibers were characterized using Raman scattering at room temperature with a green laser (wavelength = 514 nm) as the exciting radiation. The cross-sectional dimensions and area (S) were evaluated using a scanning probes microscopy (SPM) [Wang et al, 2002, 2003].

A two point probe setup was used to continuously monitor the conductance (G) in the temperature range between 300 and 1.9 K, back and forth, without any applied magnetic field. Its resistance (R) was measured from 295 K down to 15 K with a sampling interval around 0.02 K. To suppress the possible heating effect during the measurement, the constant dc current passing through the fiber was kept at 1 μA or below, and the temperature was controlled automatically. Conductance was also measured at 1.9, 3.0, 5.0, and 10.0 K while the applied magnetic field, perpendicular to the fiber, was increased or decreased continuously between -9 and 9 Tesla twice. According to a previous analysis [Rebbouillat et al, 1998], the contact resistance is much less than that of the nanofiber itself. The length L and cross section area S of the fibers were measured using an optical microscope and a scanning probe microscope (SPM) operated in tapping mode. The conductivity was finally determined using $\sigma = GL/S$.

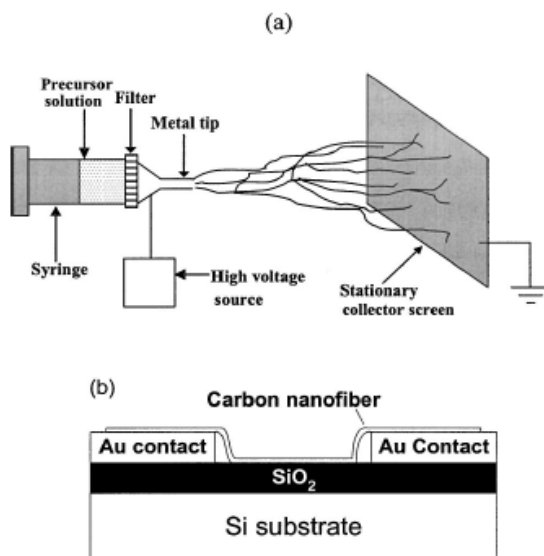


Fig. 1. Schematic of (a) homemade electrospinning setup (b) carbon nanofiber deposited on substrate

Binary Oxides: The SnO_2 fiber fabrication process was characterized by a Fourier Transform Infrared Spectrometer, equipped with a semi-demountable liquid cell with rectangular potassium bromide (KBr) windows and a universal attenuated total reflectance (UATR) sampling accessory with composite zinc selenide and diamond crystals on its top plate. The PEO powder was sampled using the UATR; the pristine $\text{C}_{22}\text{H}_{44}\text{O}_4\text{Sn}$ liquid and the polyethylene oxide/ CHCl_3 and precursor ($\text{C}_{22}\text{H}_{44}\text{O}_4\text{Sn}/\text{PEO}/\text{CHCl}_3$) solutions were sampled using the liquid cell. Since our liquids have strong IR absorption, the spacer was withdrawn from the liquid cell and the liquid samples were pressed between two KBr window plates. The produced film is estimated to be no thicker than $10\ \mu\text{m}$, thinner than the thinnest spacer commercially available ($50\ \mu\text{m}$). The as-deposited and heat-treated mats were scratched off their substrates, ground into powder and sampled using the UATR. To compensate for the high cutoff wave number ($650\ \text{cm}^{-1}$) caused by the UATR and Si substrate, the ground powders were then sampled as mulls using the liquid cell with its spacer thickness = $50\ \mu\text{m}$. Mulls were prepared by dispersing ground powders in the Nujol® (Perkin-Elmer) oil and stirring the mixture electromagnetically until a homogeneous liquid suspension was formed.

Tin Oxide Nanofibers: The synthetic procedure, is briefly recounted here to facilitate the analysis of the results in this chapter. Commercially available PEO (molecular weight 900 000) and chloroform were mixed in the ratio of 10 mg PEO/1 ml CHCl_3 and the mixture was stirred using a magnet until the homogeneous solution formed and commercial alkoxide $\text{C}_{22}\text{H}_{44}\text{O}_4\text{Sn}$ was added to the solution in a volume ratio of 2:1. The new mixture was stirred until it finally became a homogeneous solution with the appropriate viscosity. TGA and DTA on the precursor solution was conducted using platinum (Pt) pans in a simultaneous differential technique module from room temperature to $700\ ^\circ\text{C}$ at a heating rate of $10\ ^\circ\text{C}$

min⁻¹. The precursor solution, after loading into the pan, was left in the air for its solvent to evaporate until its weight became relatively stable for the thermal analysis to start. Precursor fibres and mats were electrospun using a homemade set-up [84–88] onto thermally oxidized single-crystal silicon wafers with (111) orientation, and heat-treated subsequently in air for 2 h at 200, 300, 400, 500 and 600 °C, respectively. The silicon substrates used were thermally oxidized until their surface oxide thin film had a thickness of around 180 nm. The as-deposited precursor fibres were observed under an optical microscope equipped with a digital camera. The microscope, when in its differential interference contrast (DIC) mode, can form an image which appears distinct and three-dimensional. The fibres after heat treatment were observed under a scanning electron microscope (SEM), operated at an accelerating voltage of 3–5 kV, and characterized using an x-ray diffractometer equipped with a Cu K α x-ray source and a graphite monochromator. Gold contacts of 50 μ m \times 50 μ m \times 200 nm with neighboring distance 50 μ m were thermally evaporated along one single ribbon using nickel TEM grids as masks, which were fixed by the magnetic force from a flat magnet sheet on the backside of the substrate (figures 2(a) and 2(b)). Electrical properties of single porous nanoribbons were characterized using a self-assembled system (figure 2(c)) in ambient air with a relative humidity of 90%. The sample was heated using a hot plate. A thermocouple was directly attached to the substrate and used to monitor the temperature. To create a uniform local temperature distribution around the sample, an aluminum case was used to enclose the sample. The sample was heated from 300 to 660 K and, immediately after the measurement at 660K, cooled down to 300K with the measuring temperature isochronally varied around every 10K. At each measuring temperature, the measurement was not performed until the temperature was stable for 5 min. I-V characteristics were measured using the two probe method and a semiconductor characterization system. The measuring voltage was swept cyclically, that is, from 0 \rightarrow 1V \rightarrow -1V \rightarrow 0V with \pm 0.01V steps.



Fig. 2. Deposition of Au contacts along a single SnO₂ ribbon using TEM grids as masks: (a) schematics, (b) optical micrograph of resulting sample, (c), schematics of the testing system.

Ternary and more complex oxides:

3. Comments on the experimental results:

Carbon Nanofibers: Fig. 3 shows an SEM image of the heat-treated carbon fiber. Its horizontal diameter was measured to be approximately 120 nm. Scanning probe microscopy height image analysis revealed an elliptical cross-sectional profile with approximately the same horizontal diameter of 120 nm, a vertical diameter of only 75 nm [1, Wang et al, 2003], and its area $S = 7068 \pm 200$ nm². The Raman microscattering spectrum shows two strong peaks centered on 1371 and 1588 cm⁻¹, respectively, indicating disordered and graphitic carbons in the nanofiber. The in-plane graphitic crystallite size L_a was estimated to be around 2.5 nm [2, Wang et al, 2003].

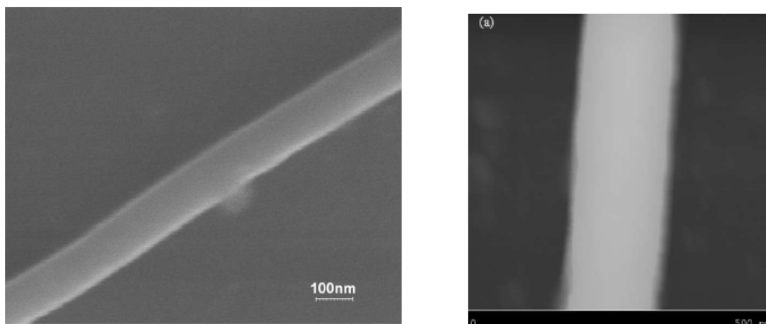


Fig. 3. SEM micrograph of carbon nanofiber

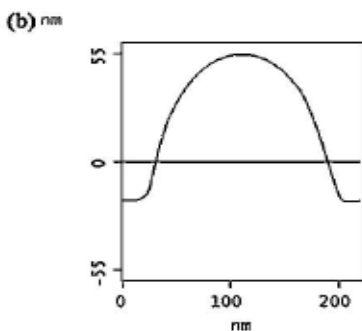


Fig. 4. (a) Scanning probe micrograph of a carbon nanofiber and (b) its average cross-section profile.

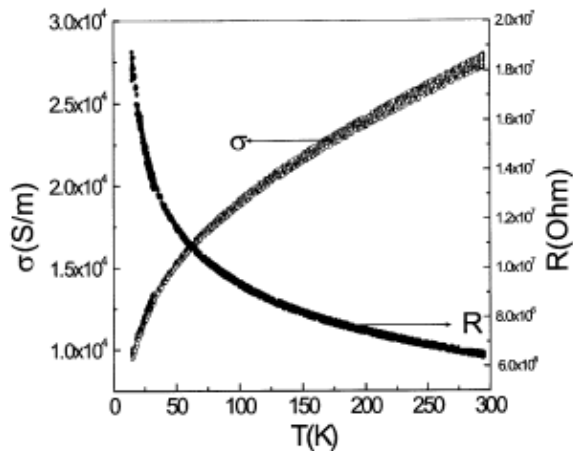


Fig. 5. Temperature dependence of R and σ

The figure above (5), shows a plot of R and σ versus temperature (T) in the range from 15 to 295 K. Note that σ increases monotonically and smoothly from 1.0×10^4 S/m at 15 K to 2.75

$\times 10^4$ S/m at 295 K, indicating the semiconducting nature of the fiber. Similar temperature dependence of conductivity was also found in carbon microfibers [Spain & Volin, 1983].

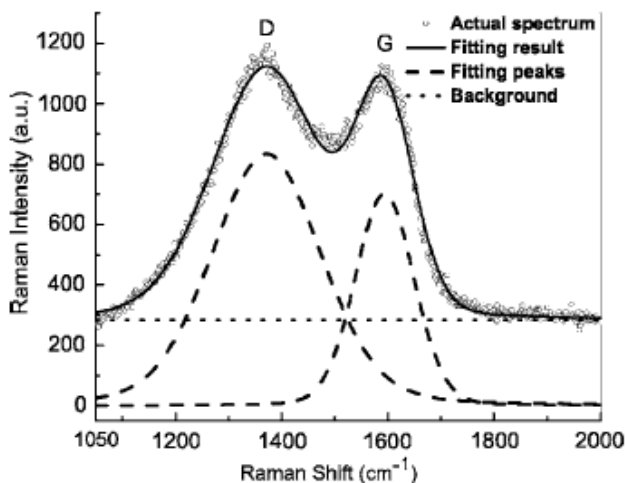


Fig. 6. Raman spectrum of the pyrolyzed fiber

Fig. 6 above, shows the Raman spectrum of the same carbon nanofibers whose G and D peaks, centered at 1371 and 1588 cm^{-1} , attest to the coexistence of disorder and graphitic carbon in the nanofibers. From the ratio of the integrated intensity of D peak to G peak, the inplane graphitic crystallite size L_a was estimated to be 2.47 ± 0.08 nm [Mott & Davies, 1979]. The bands were fitted to a Gaussian-Lorentzian shape, with their integrated intensity ratio $R=2.1$. Since MC is positive for $\text{HTT} = 1173$ K, the carrier mobility cannot be measured from the negative parabolic field dependence of MC as in the case of $\text{HTT} = 1273$ K [146] and the n value is unknown for the time being. However, n and k_{FI} values can still be estimated. At room temperature, σ value for $\text{HTT} = 1173$ K is only half of that for $\text{HTT} = 1273$ K [Fig. 5(c)]. If the ratio is attributed exclusively to the difference in n , n value for $\text{HTT} = 1173$ K will be half of that for $\text{HTT} = 1273$ K [146], i.e., 10^{25} m^{-3} , $k_{\text{FI}} \approx (3\pi^2 n)^{1/3} \approx 6 \times 10^8 \text{ m}^{-1}$, and its $k_{\text{FI}} \approx k_{\text{FI}} L_a$ is 1.2. While the fiber treated at 1273 K between 10 and 200 K, manifesting a WL regime that is not the case for the fiber treated at 1173 K, where the linear relation between $\ln \sigma(T)$ and $T^{1/2}$ [Fig. 5(d)] confirms the VRH regime between 300 and 5 K. Although such a relation cannot identify whether the VRH regime is of the Mott type (with $d=1$) or the E-S type, the turbostratic phase structure of our pregraphitic carbon fibers demands $d=2$ [Mrozowski & Chaberski, 1956], and $\sigma(T)$ with $\text{TES} = 187$ K. Using $\xi \approx L_a \approx 2$ nm, we can estimate $\epsilon_r \approx 200$. This value seems reasonable in that it lies between the metallic and insulating limits of $\epsilon_r \approx \infty$ and $\epsilon_r \approx 10$, respectively.

Fig. 7(a) shows the magnetoresistance MR, defined as $\text{MR} = \rho(B)/\rho(0) - 1$, and the magnetoconductivity $\text{MC} = \sigma(B)/\sigma(0) - 1$ of the fibers at temperatures of 1.9, 3.0, 5.0 and 10 K with magnetic field B from -9 to 9 T. At all four investigated temperatures, the MR is negative. Its magnitude increases with an increase in B and a decrease in T . It is noteworthy that $\text{MR} = -0.75$ at $T = 1.9$ K and $B = 9$ T, one of the largest negative magnetoresistance known to the authors. Since $|\text{MR}|$ is quite large, $\text{MR} \approx (\text{MC})^{-1}$ is not always valid. The

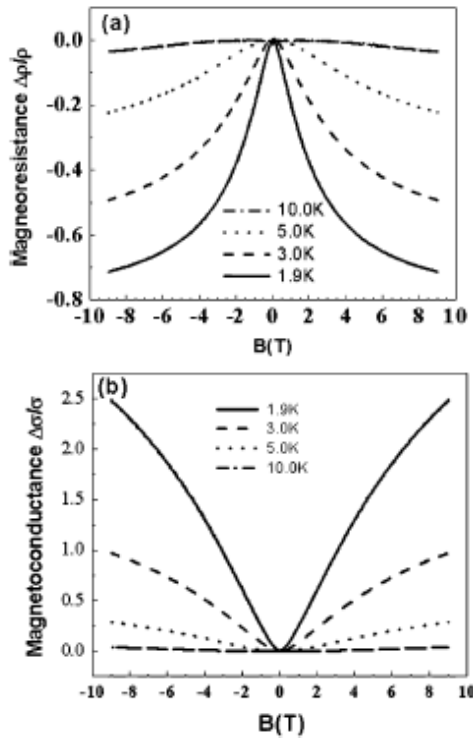


Fig. 7. (a) Large negative magnetoresistance and (b) positive magnetoconductance of carbon fibers with magnetic field from -9 to 9 T.

magnetic field dependence of magnetoresistance for most electronic systems exhibiting 2-D weak localization is relatively easy to understand. In carbon fibers, however the origin is *a priori* not obvious. Bright attributed the origin to the turbostatic nature of the samples, which should have an electronic structure nearly the same as that of 2-D graphite. In the 2-D regime, the correction to the sheet conductance G produced with the magnetic field B perpendicular to the plane of the 2-D carrier system is given by the following expression [Bayot et al, 1989, 1990], [Rosenbaum, 1985]:

$$G(B, T) = G_{\infty} + \frac{e^2}{\pi h} \left[\frac{3}{2} \Psi \left(\frac{1}{2} + \frac{B_2}{B} \right) - \Psi \left(\frac{1}{2} + \frac{B_1}{B} \right) - \frac{1}{2} \Psi \left(\frac{1}{2} + \frac{B_3}{B} \right) \right], \tag{4}$$

$$B_1 = B_0 + B_{s.o.} + B_s,$$

$$B_2 = B_i(T) + \frac{4}{3} B_{s.o.} + \frac{2}{3} B_s,$$

$$B_3 = B_i(T) + 2 B_s,$$

G_∞ is the sheet conductance at infinite magnetic field, or as calculated in the classical Boltzmann formulation of the transport theory; ψ is digamma function, and B_k ($k=0, l, s, \text{ s.o.}$) represents the characteristic field associated with the scattering mechanism κ standing for elastic scattering (o), inelastic scattering (i), magnetic impurity scattering (s) and spin-orbit coupling (s.o.). Therefore, the magnetoconductance takes the form

$$\text{MC} = \eta(T) \left[\frac{3}{2} \Psi \left(\frac{1}{2} + \frac{B_2}{B} \right) - \Psi \left(\frac{1}{2} + \frac{B_1}{B} \right) - \frac{1}{2} \Psi \left(\frac{1}{2} + \frac{B_3}{B} \right) - \ln \frac{B_2^{3/2}}{B_1 B_3^{1/2}} \right], \quad \text{where} \quad \eta(T) = \frac{e^2}{\pi h G(0, T)}. \quad (5)$$

Given a temperature T , (5) contains only four unknown parameters: $\eta(T)$, B_1 , B_2 , and B_3 . They can be derived from a nonlinear fitting. The results show that B_2 and B_3 have very close fitting values. In fact, their difference is less than their respective fitting errors. This indicates that both $B_{s,o}$ and B_s are very small, i.e., both magnetic impurity scattering and spin-orbit coupling are very weak. For simplicity, we assume $B_{s,o} \approx B_s \approx 0$, and $B_1 = B_0$, $B_2 = B_3 = B_i(T)$. Then (5) can be simplified as

$$\text{MC} = \eta(T) \left[\Psi \left(\frac{1}{2} + \frac{B_2}{B} \right) - \Psi \left(\frac{1}{2} + \frac{B_1}{B} \right) - \ln \frac{B_2}{B_1} \right]. \quad (6)$$

Nonlinear curve fitting using (6) and Mathematica software (shown in Fig. 8) showed that B_i increases with T , i.e., the inelastic scattering intensifies when the temperature increases. The temperature dependence of zero field conductivity can be considered in parallel to the modified STB model [Wang & Santiago-Aviles, 2003], which accounts for the conductivity phenomenological, several other models can explain the temperature dependence of the conductivity, namely: 1) 2-D weak localization model: According to the 2-D weak localization model [Lee & Ramakrishnan, 1985; Langer et al, 1996]

$$\sigma(T) = \sigma(0) + \frac{e^2}{2\pi^2 \hbar} \ln \left[1 + \left(\frac{T}{T_C(B, \tau_s)} \right)^p \right] \quad (7)$$

where $\sigma(0)$ and $T_C(B, \tau_s)$ are two constants. If (7) is used to fit the temperature dependence of the zero field conductivity, we obtain, $\sigma(0) = 0$, and $p = 1.15$ (Fig. 9). The value $p=1.15$ is in agreement with the previous results of $p \approx 1.00$ in carbon microfibers [Bayot et al, 1989] and multiwalled carbon nanotube [Langer et al, 1996]. It indicates that the dominating inelastic scattering mechanism is likely to be disorder enhanced electron-electron scattering in 2-D system.

2) Variable range hopping model: This phenomenon occurs in highly disordered materials because the distribution of energy states makes it more favorable to hop to a distant empty state of nearly the appropriate energy than to a nearby empty state that has a much higher energy level. Because of the high resistivity and lack of long-range order of the fiber, one

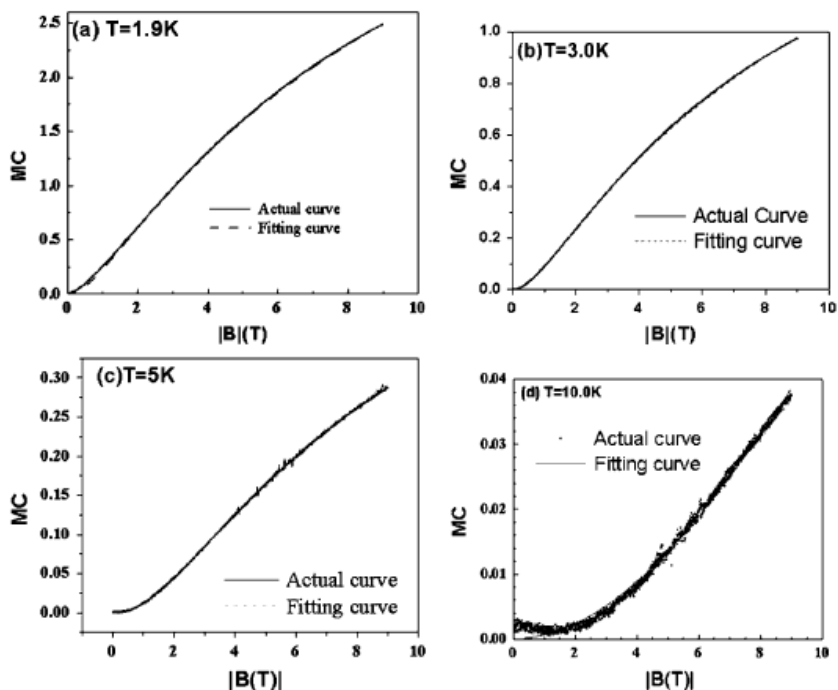


Fig. 8. Comparison of magnetoconductance fitting curves [using (6)] with experimental curves.

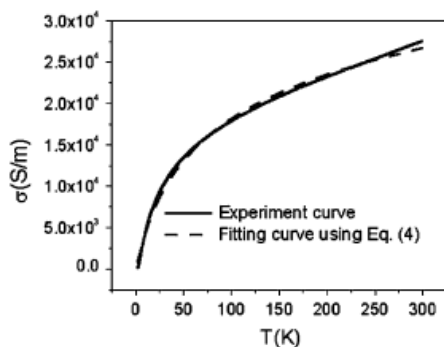


Fig. 9. Fitting of conductivity curve to (7).

would expect that the electrical conduction would result from a hopping mechanism. The dimensionality enters the equation during the summing of the available states. For a d-dimensional system [Mott & Davies, 1979]

$$\sigma(T) = A \exp \left[-\frac{B}{T^{1/(d+1)}} \right] \tag{8}$$

where $d = 1, 2, 3$, and A, B are two constants. Since there is controversy about the dimensionality of the carbon fibers with respect to variable range hopping, a good three-parameter fit to all the data was found by least square fitting of the data to (8)(Fig. 11). The fitting results $d = 0.295$ indicates that the dimensionality of hopping lies between 2 and 3, or that $d = 2$ and $d = 3$ coexist.

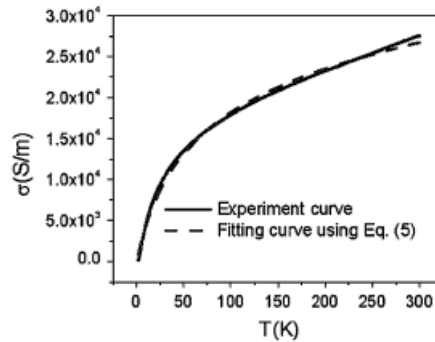


Fig. 10. Fitting of conductivity curve to (5).

Tunneling can be considered as part of transport, the tunneling model was developed for metallic particles imbedded in a highly resistive matrix but the only essential feature of the metallic particles is that the conduction electrons therein are delocalized. As revealed by XRD and Raman spectra, the graphite domains within our carbon nanofibers have a size of 1 to 2 nm [3, Wang et al, 2003]. Since electrons on the small fully carbonized basic units fit this criterion, it is not unreasonable that the model may apply to the investigated fibers. For dc conduction, electron tunnel between the charging centers imbedded in a highly resistive matrix of totally disordered carbon might be plausible. When the electric field is low, the conduction is ohmic resulting in thermally activated charge carriers hopping to the nearest neighbor-charging center. For high-electric fields, the conduction is highly nonohmic and is the result of field-induced tunneling. The conductivity in this model has the same form as 1-d variable range hopping [Abeles et al, 1975]

$$\sigma(T) = A_1 \exp \left[-\frac{B_1}{T^{1/2}} \right] \quad (9)$$

Where A_1 and B_1 are two constants. If the $\sigma(T)$ versus T curve is fit to (9) [Fig. 11], we obtain $A_1 = 41172$ S/m, $B_1 = 7.92617$ K^{1/2}. It seems reasonable to try to fit the data to a model in which 3-D variable range hopping and tunneling between domains, in which the electrons are delocalized, coexist. The conductivity for such a case is

$$\sigma(T) = A \exp \left[-\frac{B}{T^{1/(d+1)}} \right] + A_1 \exp \left[-\frac{B_1}{T^{1/2}} \right]. \quad (10)$$

Fig. 12 shows the results of fitting the data to (10). The fitting is excellent. The figure also shows the curves for the two components. They indicate that the conduction is mostly undertaken by a tunneling mechanism. It increases the convexly with the temperature, the

hopping mechanism accounting for only a small fraction of the total (its contribution to the conductivity increases concavely with the temperature). As such, the hopping mechanism can be excluded from the main transport mechanism(s) in the investigated carbon fiber.

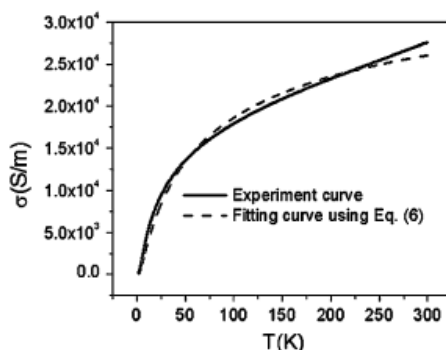


Fig. 11. Fitting of conductivity curve to (9)

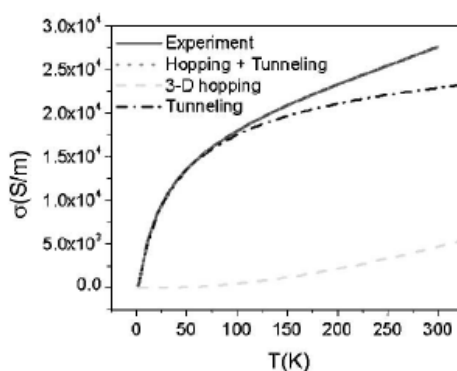


Fig. 12. Fitting of conductivity to (7)

Since both (7) and (9) fit the experimental σ versus T curve quite well, the fitting alone seems not enough to determine whether the main transport mechanism is 2-D weak localization effect, or the tunneling mechanism. However, the good description of the T - and B -dependence of the large MR that can be done using 2-D weak localization effect indicates that the same effect is mainly responsible for the T -dependence of the conductivity. This harmonizes with the low-electrical field setup during the conductance measurement. The voltage applied between the two conducting pads, separated by a distance of 1 mm, is 0.03-0.6 V. So the average electrical field in the carbon nanofiber between the two pads is 30-600 V/m, not strong enough for the tunneling mechanism to dominate.

Binary oxides: Previously we discussed the precursor mixing process for SnO_2 . Here, Figure 13 shows thermal analysis curves of the precursor solution. As the temperature increases from room temperature, the weight decreases steadily at first and then slows between 100 and 150 °C, beyond which the weight decreases drastically to 5.2% around 270 °C, where the weight-loss rate drops sharply to a very low level until 385 °C. Above this value the weight

remains practically unchanged. The corresponding derivative TG (DTG) curve also indicates three temperature regions in term of the weight loss, peaked around 60, 246 and 301 °C, respectively. The DTA curve, on the other hand, reveals two partially overlapping processes with their exothermic effect ranging from 220 °C to 280 °C (peaked around 263 °C) and from 280 °C to 390 °C (peaked around 345 °C), respectively. Combining the results, one can see that the TG, DTG and DT curves point out four distinct temperature regions with their respective overall changes: CHCl_3 evaporates from room temperature to 100 °C (note that 60 °C is its boiling point in air); PEO and $\text{C}_{22}\text{H}_{44}\text{O}_4\text{Sn}$ decompose rapidly into an intermediate product between 220 and 300 °C; the intermediate product undergoes a minor weight loss between 300 and 385 °C; and no major chemical reaction occurs with weight change above 400 °C.

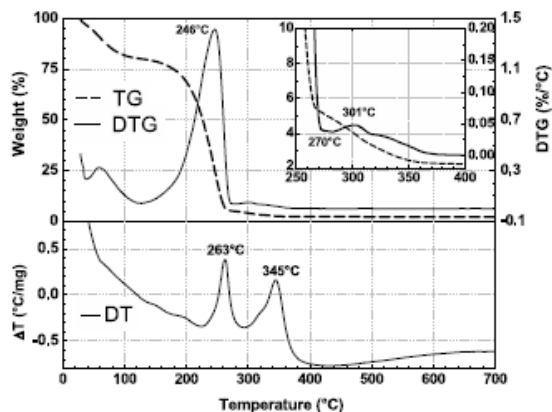


Fig. 13. Thermal analysis (TG, DTG and DT) curves of the precursor solution. The inset highlights TG and DTG curves between 250 and 400 °C

The XRD spectra shown in figure 14 indicate that the samples were amorphous and the 100, 101, 200 and 211 characteristic peaks of the rutile-structured SnO_2 [JCPDS cards] do not emerge until 400 °C. The peaks become more distinct as the heat treatment temperature rises. Additional peaks indexed to the 220 and 310 planes, indiscernible after the heat treatment at and below 500 °C, became evident at 600 °C although they are not as strong and distinct as the others. Except for the Si (111) peak [JCPDS cards] from the substrate in the spectrum of 500 °C, all peaks are characteristic of rutile-structured SnO_2 . The multiple diffraction peaks reflect the polycrystalline nature of the sample. Their relative intensity, similar to that in the JCPDF card of rutile-structured SnO_2 , indicates no obvious texture (preferential orientation) of crystallites within the samples. The combination of thermal analysis and XRD results gives us a clearer picture of the process: while the exothermic process between 220 and 300 °C does not produce any crystallization, the other process, between 300 and 385 °C, results in the incipient rutile lattice. Above 400 °C, the major change is the further development of the incipient lattice, i.e. phase transformation without obvious weight or stoichiometric change. Optical micrographs show precursor fibres of smooth surfaces with indent belts (figures 15(a) and (b)) along their length axis, whose formation mechanism is under investigation. The equal-thickness interference fringes in figure 21(a) clearly indicate that the height/thickness of the precursor fiber varies along the

direction of the horizontal diameter. Optical microscopic observation also revealed that the final SnO_2 fibres have typical lengths of up to a few millimeters. SEM observation further revealed that the fibres are porous and their diameters range from 100 nm to 40 μm (figures 15(c)–(f)).

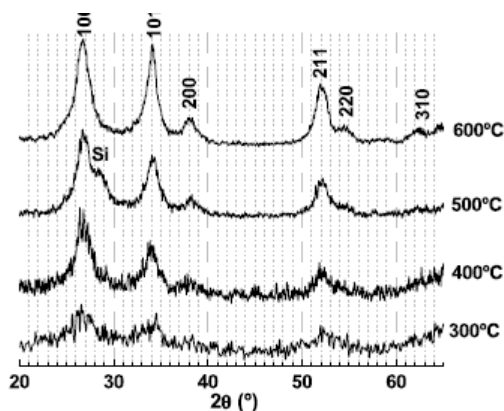


Fig. 14. X-ray diffraction spectra of mat samples heat treated from 300 to 600 °C. The indexes were assigned as the rutile structure of SnO_2 according to [JCPDS cards]. The extra peak at 500 °C is due to (111) diffraction of the single-crystal Si substrate according to [JCPDS cards]. The mat sample heat treated at 500 °C was not dense and thick enough for the diffracted x-ray by the Si substrate not to be detected.

The most porous regions in the final fibres lie in the indent bands of the precursor fibres. We are investigating how the former evolve from the latter and trying to quantitatively measure the surface area of our porous fibres using the BET or any other pertinent method [Brunauer et al, 1938]. The difficulty of the measurement lies in synthesizing enough of the material to do the isotherms and separating our fibres from their substrates without changing their porous morphology. Figure 15(a) shows FTIR spectra of the starting chemicals PEO, CHCl_3 and $\text{C}_{22}\text{H}_{44}\text{O}_4\text{Sn}$ with their major absorption bands tentatively assigned. The assigning for CHCl_3 was easy as it and its IR spectrum are well known and widely published [Silverstein & Webster, 1998]. The assigning for PEO was helped by [Ratna et al, 2006] and [Deng et al, 2006]. The work for $\text{C}_{22}\text{H}_{44}\text{O}_4\text{Sn}$ was the most difficult: it is rarely reported and its IR spectrum is unavailable in the literature.

In the FTIR spectrum of the as-deposited precursor mats (figure 16(a)), there is no chloroform absorption bands, indicating a total evaporation of the volatile solvent during the electrospinning. In fact, the as-deposited spectrum is similar to that of pure $\text{C}_{22}\text{H}_{44}\text{O}_4\text{Sn}$ except for the sharp bands centred around 1553 and 1411 cm^{-1} . The former 'extra' band was weakened and shifted to 1530 cm^{-1} by the heat treatment at 200 °C, which, however, did not change other major characteristic bands except for the shift of the bands below 800 cm^{-1} toward lower wavenumber. Significant changes occur after the heat treatment at 300 °C, where the bands of such organic groups as methyl ($-\text{CH}_3$), methylene ($-\text{CH}_2$), methylidyne ($-\text{CH}$), carbonyl ($-\text{C}=\text{O}$) and hydroxyl ($-\text{O}-\text{H}$) almost disappear (figure 16(b)), suggesting their decomposition. Meanwhile, there appears a band around 760–730 cm^{-1} , which can be attributed to the asymmetric Sn–O–Sn stretching [Almaric-Popescu, 2001], and the Sn–C band merges with the band previously around 634 cm^{-1} into a broad band centred around

Thank You for previewing this eBook

You can read the full version of this eBook in different formats:

- HTML (Free /Available to everyone)
- PDF / TXT (Available to V.I.P. members. Free Standard members can access up to 5 PDF/TXT eBooks per month each month)
- Epub & Mobipocket (Exclusive to V.I.P. members)

To download this full book, simply select the format you desire below

